APPLIED SCIENCES AND ENGINEERING

Lifetime-configurable soft robots via photodegradable silicone elastomer composites

Min-Ha Oh[1]†, Young-Hwan Kim[1]†, Seung-Min Lee[1]†, Gyeong-Seok Hwang[2], Kyung-Sub Kim[1], Yoon-Nam Kim[1], Jae-Young Bae[1], Ju-Young Kim[2], Ju-Yong Lee[1], Yu-Chan Kim[3,4], Sang Yup Kim[5]*, Seung-Kyun Kang[1,6,7]*

Developing soft robots that can control their own life cycle and degrade on-demand while maintaining hyperelasticity is a notable research challenge. On-demand degradable soft robots, which conserve their original functionality during operation and rapidly degrade under specific external stimulation, present the opportunity to self-direct the disappearance of temporary robots. This study proposes soft robots and materials that exhibit excellent mechanical stretchability and can degrade under ultraviolet light by mixing a fluoride-generating diphenyliodonium hexafluorophosphate with a silicone resin. Spectroscopic analysis revealed the mechanism of Si—O—Si backbone cleavage using fluoride ion (F^-) and thermal analysis indicated accelerated decomposition at elevated temperatures. In addition, we demonstrated a robotics application by fabricating electronics integrated gaiting robot and a fully closed-loop trigger disintegration robot for autonomous, application-oriented functionalities. This study provides a simple yet novel strategy for designing life cycle mimicking soft robotics that can be applied to reduce soft robotics waste, explore hazardous areas, and ensure hardware security with on-demand destructive material platforms.

INTRODUCTION

Soft robotic materials with hyperelasticity and tunable functionalities have been an integral part of soft robotics (*1*, *2*). Unlike conventional robots with limited degrees of freedom, soft robots demonstrate advanced functional adaptability and enable convoluted movements, such as delicate handling of vulnerable objects or adapting to uncertain environments (*3*, *4*). The rapid evolution of soft robots improved their capability of mimicking the individual functions of biological systems and emulating the life cycle of living organisms, such as growth (*5*, *6*), healing (*7*, *8*, *9*), transition (*10*), transformation (*11*), and death (*12*). Considering the life cycle mimicry by robotic systems, the "death" and "disposal" of soft robots after their operational lifetime have gained wide attention in terms of creating a sustainable environment for future robotic systems (*13*). Transient soft robots, whose components degrade or dissolve in a controlled manner, are emerging as a solution for the effective death management of soft robots that are no longer needed. In particular, transient soft robots have unique applications as unrecoverable and vanishing robots for hardware security in military operations like scouting, invasion, or transport, without being exposed to enemies (*14*, *15*); exploration of dangerous location such as deep sea or radioactive areas where the retrieval of robots is expensive or unavailable (*16*–*20*). However, the biggest bottleneck in the disposal of soft robots is the management of their body material: a thermoset silicone elastomer. Although the low modulus, high stretchability, and processability of silicone elastomers make them a gold-standard body material of soft robotics, the disposal of silicone elastomer is difficult owing to their highly cross-linked network structure, which allows silicone elastomers to bear ~300°C of heat, acids or alkaline with extreme pH conditions, and other hazardous chemicals (*21*, *22*). This stability makes bare silicone elastomers unsuitable for decomposable robots, resulting in alternative application fields. In addition, degradable elastomers spanning natural and synthetic polymers have recently gained high interest. Thermoplastic elastomers, such as polyurethanes, can be used as candidate materials for constructing soft robots as they exhibit elastomeric mechanical properties. However, in the case of these thermoplastic elastomers, physical melting occurs because of an increase in chain mobility caused by the distance between polymer chains becoming farther apart, rather than a chemical decomposition reaction using cleavage of polymer chains. This means that, after the melting reaction of the polymer, the material exists again as polyurethane, which can be described as a recoverable state rather than complete decomposition. Furthermore, in the case of thermoplastic polyurethane (TPU), which achieves elastic properties through physical cross-linking (van der Waals interaction), it exhibits a relatively narrow elastic region of approximately ~20% (*23*). On the other hand, silicone, which uses chemical cross-linking (covalent bonding), exhibits an elastic region of around 300 to 500% (*24*).

Previous studies on fully degradable soft robotic materials depended on passive transient elastomers such as poly(glycol sebacate) (PGS) and gelatin-based biogels. The PGS-$CaCo_3$ polymer was used to fabricate accordion-style pneumatic actuators and demonstrated full degradability after being buried in compost (*25*).

---

[1] Department of Materials Science and Engineering, Seoul National University, 1 Gwanak-ro, Gwanak-gu, Seoul 08826, Republic of Korea. [2] Department of Materials Science and Engineering, UNIST (Ulsan National Institute of Science and Technology), Ulsan 44919, Republic of Korea. [3] Center for Biomaterials, Biomedical Research Institute, Korea Institute of Science and Technology (KIST), Seoul 02792, Republic of Korea. [4] Division of Bio-Medical Science and Technology, KIST School, Korea University of Science and Technology, Seoul 02792, Republic of Korea. [5] Department of Mechanical Engineering, Sogang University, 35 Baekbeom-ro, Mapo-gu, Seoul 04107, Republic of Korea. [6] Research Institute of Advanced Materials (RIAM), Seoul National University, 1 Gwanak-ro, Gwanak-gu, Seoul 08826, Republic of Korea. [7] Nano Systems Institute SOFT Foundry, Seoul National University, 1 Gwanak-ro, Gwanak-gu, Seoul 08826, Republic of Korea.
*Corresponding author. Email: kskg7227@snu.ac.kr (S-K.K.); sangyupkim@sogang.ac.kr (S.Y.K)
†These authors contributed equally to this work.

Gelatin biogel has also been applied to electronic skins, soft actuators, and electronic sensor patches with excellent tunability, mechanical properties, and transience in deionized (DI) water (*26*). However, these examples are still considered passive degradation considering that the degradation is based on the hydrolysis rate of the materials. This type of robotic material degradation has two major drawbacks: (i) the performance of the materials or systems continuously degrades along with their decomposition and (ii) the system lifetime is predetermined by the initial thickness and the environmental condition, usually without further controllability (*27*).

In contrast, on-demand transient soft robotic materials, which are highly stable yet rapidly degradable under specific external stimuli, are expected to overcome such drawbacks with their innate stimulus-responsive degradability. Unlike passive transient robots that undergo degradation immediately upon operation due to immediate interaction with the surrounding environment, on-demand transient robots can initiate the degradation at a certain time frame without functional deterioration during operation, thereby enabling novel tasks such as (i) high and stable performance of robots without functional degradation during their operation period, (ii) self-directed disappearance of temporary biomedical actuators after treatment, and (iii) the programmable life cycle of special-purpose robots. Self-immolative polymers, which have weak chemical bonding energy, resulting in chains that easily disintegrate under external conditions (*28*), are considered potential candidates for on-demand transient robotics. The Fourier transform infrared (FTIR) and nuclear magnetic resonance (NMR) analyses are conducted. However, such materials have poor flexibility and stretchability and unstable under ambient conditions as they exhibit low ceiling temperature (T_c) (*29*, *30*). For example, polyphthalaldehydes (PPAs) are the most widely used self-immolative polymers but have a Young's modulus of 2.5 to 4.5 GPa, fracture strain of 1.5 to 2%, and low ceiling temperature (T_c) of −45°C (*31*).

Here, we propose on-demand transient and hyperelastic robotic materials for lifetime configurable soft robots by dispensing a photoinduced fluoride-generating diphenyliodonium hexafluorophosphate (DPI-HFP) to various silicone resins (Sylgard-184 and Ecoflex 00-30). In addition to the hyperelasticity and simple processability that original silicone resins have, the DPI-HFP/silicone composite realizes ultraviolet (UV) triggerable transient platform for soft robotics. Spectroscopic and thermal analyses revealed the degradation mechanism and kinetics of the Si—O—Si backbone cleavage initiated by fluoride ion (F^-) generated because of exposure to UV light. Furthermore, we fabricated a highly deformable and fully degradable gaiting robot and demonstrated it in a hypothetical scouting scenario. We integrated various electronics devices such as strain, temperature, and UV sensors to measure the external signals. When the robot was exposed to UV light (365 nm), it completely disintegrated, leaving behind an oily liquid residue of decomposed silicone composite and thin film electronics; as a result, it can no longer operate. The material presented in this study demonstrates the effective translation of conventional Si—O–based silicone soft robotics to a life cycle controllable form by combining them with an on-demand transient DPI-HFP/silicone composite.

RESULTS

Overview of transient elastomer composites and lifetime-configurable soft robots

Soft robots constructed with transient silicone composites can achieve diverse actuations due to their superior mechanical properties and can also have a configurable lifetime based on the disintegration of the material under specific external stimuli. Therefore, we established a strategy for designing transient silicone composites, including fabrication, application, and disintegration (Fig. 1). The on-demand transient material was fabricated by adding fluoride ion-emitting diphenyliodonium hexafluorophosphate (DPI-HFP) to uncured commercial silicone resin (Ecoflex 00-30 and Sylgard-184) (Fig. 1A). The desired morphology of the DPI-HFP/silicone composite was achieved by pouring the DPI-HFP/silicone mixture into a polylactic acid (PLA) mold and curing at 60°C for 30 min. Upon exposure to UV light, the DPI-HFP releases F^- ions, cleaves the Si—O backbone, and converts the composite into an oily liquid. A gating robot composed of DPI-HFP/silicone was constructed as a representative application scheme (Fig. 1B). Under certain scenarios wherein disintegration is desired, including mission completion, discovery by enemies, or disposal requiring volume reduction, the robot can be exposed to UV light and disintegrate into an unrecoverable form.

The sequential photographs shown in Fig. 1C demonstrate the on-demand transient behavior of the DPI-HFP/silicone gaiting robot. Applying UV light (365 nm, 30 min) followed by heat (120°C, 60 min) leads to complete decomposition through a phase transition from a cross-linked solid state to a de–cross-linked oily liquid state. External heat is first transferred from the underlying hot plate to the robot feet and then dissipated throughout the body of the robot. The last image shows the complete degradation of the on-demand transient DPI-HFP/silicone gaiting robot, decomposing into an oily liquid state.

Decomposition chemistry of DPI-HFP/silicone composites

Figure 2 shows the decomposition mechanism of DPI-HFP/silicone composite stated in Fig. 1 via spectroscopic analysis. Figure 2A illustrates the decomposition mechanism, wherein the key to on-demand transience lies in the formation of F^- ions from UV-exposed DPI-HFP. During decomposition, the diphenyliodonium cations of DPI-HFP undergo homolytic cleavage upon UV irradiation and yield phenyliodonium radical cations (*32*). These phenyliodonium radical cations attack and receive the protons available in their environment to form iodobenzene cations (*33*). The PF_6 anions of DPI-HFP remove the protons from iodobenzene cations, leading to the formation of HPF_6 (*34*, *35*) as C—I bond energy (26 to 27 kJ/mol) is easily cleaved by UV irradiation. This HPF_6 is highly unstable under ambient conditions; it naturally decomposes and yields protons, fluoride ions, and PF_5 as the final products of photolysis (*36*, *37*). Here, the concentration of F^- ions generated from DPI-HFP at a given UV exposure time is predictable in principle (details are provided in supplementary text S1). These F^- ions cleave the Si—O backbones of silicone elastomers as a result of a thermodynamic driving force; in other words, the bond energy of Si—F (565 kJ/mol) is greater than that of Si—O (452 kJ/mol) (*38*). This leads to the fragmentation of the organosilicon network of the silicone elastomer matrix and converting the solid elastomer into an oily liquid.

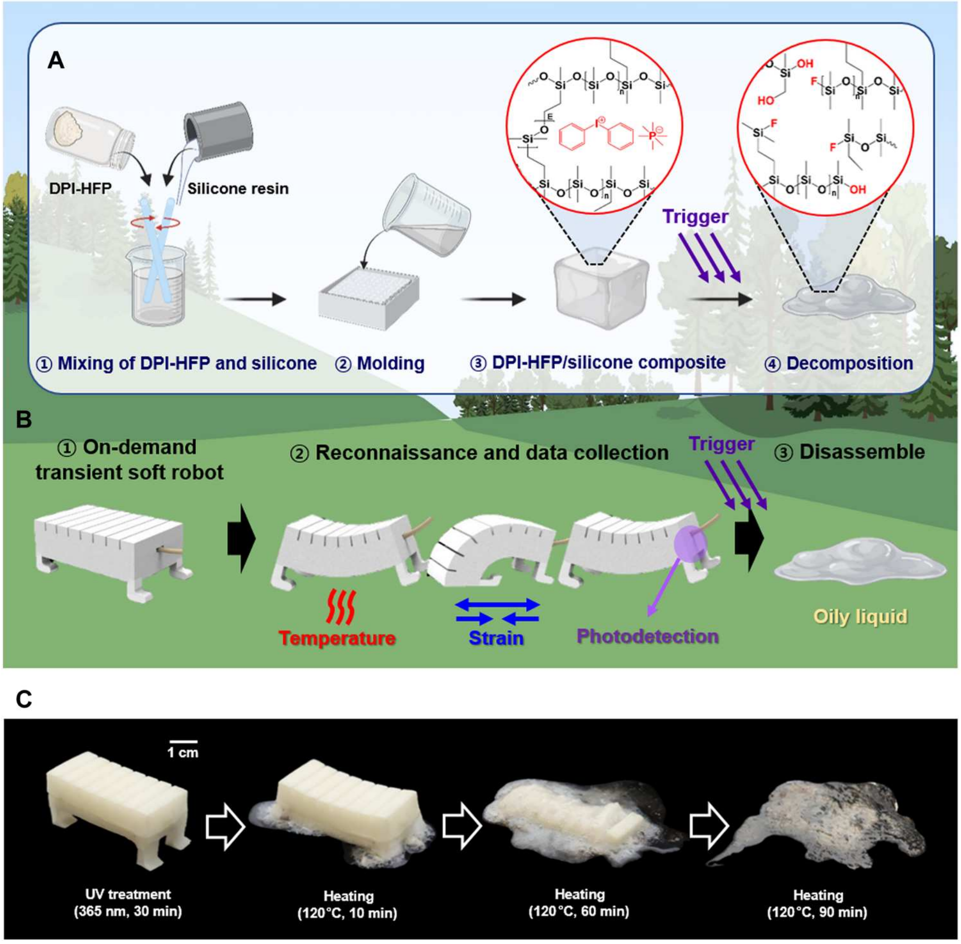

Fig. 1. Overview of transient DPI-HFP/silicone composites and a lifetime configurable soft robot. (**A**) Fabrication process of a transient DPI-HFP/silicone elastomer composite and its decomposition response upon application of a trigger. (**B**) Illustration of a lifetime configurable gaiting robot capable of sensing the surrounding environment and disassembling the entire system via trigger application whenever necessary. (**C**) Time-lapse image of the gaiting robot undergoing decomposition at 120°C for 30 min after exposure to UV light (365 nm).

Figures 2 (B to G) (DPI-HFP/Ecoflex 00-30) and fig. S1 (A to C) (DPI-HFP/Sylgard-184) show the spectroscopic observations of DPI-HFP/silicone composite before and after the trigger. The T_2 relaxation time of DPI-HFP/Ecoflex 00-30 obtained using solid-state ^{1}H-NMR relaxometry was used to compare the cross-linking density of the silicone elastomer before and after UV exposure (Fig. 2B). An increase in the T_2 relaxation time of a polymer, which is inversely proportional to the cross-linking density, indicates that the UV light leads to the de–cross-linking and fragmentation of the organosilicon network (*39*). The FTIR spectra in Fig. 2C show a decrease in the peak of the Si─O─Si bond (1013 cm^{-1}) after UV light exposure due to Si─O bond cleavage via F$^-$ ions. In addition, the peak of the Si─CH$_3$ bond (792 cm^{-1}) decreased due to the presence of the Pt catalyst in the silicone elastomers for addition curing (*40*, *41*). The ^{29}Si-NMR spectra in Fig. 2 (D and E) show a decrease in the in-chain Si peak [−22.56 parts per million (ppm)] and the end-of-chain Si peak (6.56 ppm), respectively, as a result of the Si─O bond cleavage. Comparing the ^{29}Si-NMR spectra in Fig. 2 (F and G) showed changes in the chemical bonds before and after the UV trigger. Only Si─O bond peaks (−23 ppm) were observed in the ^{29}Si-NMR spectra before the UV trigger (Fig. 2F). As UV exposure generated fluoride ions, which attack the Si─O bonds, Si─F bond peaks (−8 ppm) and Si─OH bond peaks (−11.6 ppm) emerge in addition to the Si─O bond peaks (Fig. 2G). Additional ^{29}Si-NMR analyses conducted on Sylgard-184 (fig. S2B) indicated similar trends before and after the UV trigger.

Ecoflex 00-30 and Sylgard-184 are commonly used variations of linear chain poly(dimethylsiloxane) (PDMS), which may contain significant amounts of additive materials (such as silica) that contribute to the insolubility of the residue in organic solvents. To address this, in fig. S2A, we used a model system by combining DPI-HFP with linear chain PDMS (DPI-HFP/PDMS). The ^{29}Si-NMR analysis of the linear PDMS [number-average molecular weight (M_n) = 139,000] demonstrated a similar trend before and after the UV trigger (fig. S2A). Further analysis of the residue resulting from DPI-HFP/PDMS provided insights into the specific components generated by the trigger (fig. S3, A and B). The FTIR spectrum in fig. S3A illustrates that DPI-HFP/PDMS experienced the same cleavage of Si─O─Si and Si─CH$_3$ as observed in DPI-HFP/Ecoflex 00-30 (Fig. 2C) and DPI-HFP/Sylgard-184 (fig. S1A). The ^{29}Si-NMR spectra in fig. S3B indicates the exact

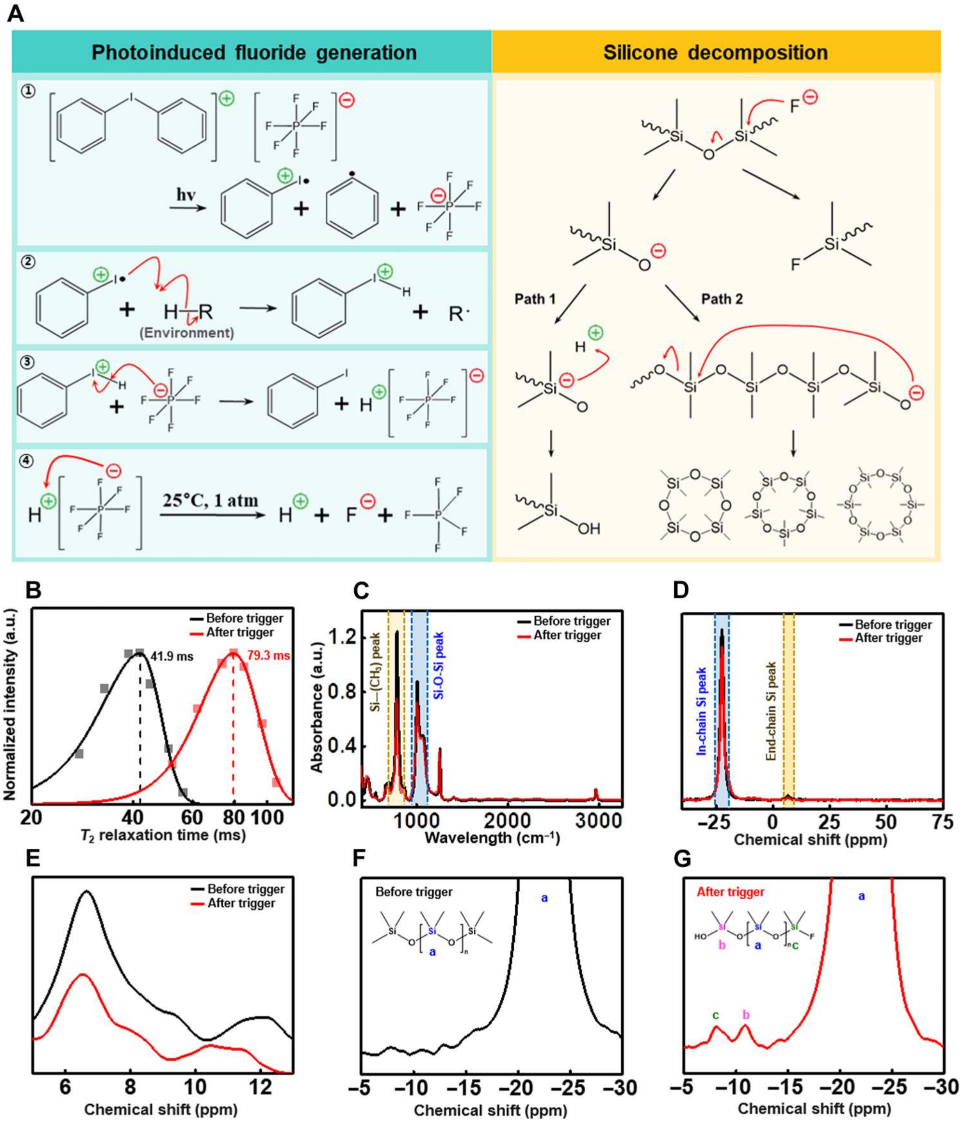

Fig. 2. Decomposition chemistry of DPI-HFP/silicone composites that uses photo-induced fluoride. (**A**) Schematic of the photo-triggered decomposition of the DPI-HFP/silicone composites. The exposure of DPI-HFP to UV generates fluoride species (left), which subsequently results in Si—O bond cleavage to decompose the silicone elastomer (right). (**B**) Transverse relaxation time (T_2) distributions of DPI-HFP/Ecoflex 00-30 using solid-state ^{1}H-NMR. The T_2 relaxation time increases after applying UV and heat trigger. (**C**) FTIR spectra of DPI-HFP/Ecoflex 00-30 show an absorbance decrease in the Si—CH_3 peak (792 cm^{-1}) and the Si—O—Si peak (1013 cm^{-1}) after applying the trigger. a.u.(arbitrary unit). (**D**) Solid-state ^{29}Si-NMR spectra of DPI-HFP/Ecoflex 00-30 showing that the intensity decreases in the Si—CH_3 peak (−22.56 ppm) and Si—O—Si peak (6.56 ppm) after applying the trigger. (**E**) Magnified and rescaled view of the ^{29}Si-NMR spectra of DPI-HFP/Ecoflex 00-30 after applying the trigger. A significant decrease is visible in the Si—O—Si peak (6.56 ppm). (**F**) Solid-state ^{29}Si-NMR spectra of DPI-HFP/Ecoflex 00-30 before application of the trigger. (**G**) Solid-state ^{29}Si-NMR spectra of DPI-HFP/Ecoflex 00-30 after application of the trigger, showing the formation of cyclic hydroxyl- and fluoride-terminated PDMS chains. Here, peaks attributed to cyclic siloxane compounds are buried in the large Si—O—Si peak, and cyclic siloxane peaks are not observed owing to the innate peak broadening of solid-state NMR.

components and ratios resulting from the trigger: cyclic siloxane compounds octamethylcyclotetrasiloxane (D4), decamethylcyclopentasiloxane (D5), and dodecamethylcyclopentasiloxane (D6) and shortened hydroxyl- and fluorine-terminated PDMS. Furthermore, the formation of shortened linear PDMS chains and cyclic siloxane compounds was confirmed from the decrease in the average molecular weight (M.W.) from 104 to 105 g/mol to 102 to 103 g/mol, as measured by gel permeation chromatography (GPC) performed before and after the application of the trigger (fig. S3B). The formation of hydroxyl- and fluorine-terminated PDMS is consistent with the mechanism suggested in Fig. 2A, and their further backbiting-mediated decomposition into cyclic siloxane compounds is consistent with previous results on the decomposition of PDMS with fluoride species (*42*, *43*). Although the cyclic siloxane compounds were not visible due to innate peak broadening and resolution limit of solid-state NMR, the same compounds appeared in the residues of DPI-HFP/Ecoflex 00-30 (Fig. 2G) and DPI-HFP/Sylgard-184 (fig. S2B). In contrast, cyclic siloxane compounds are recyclable (*32*, *44*), and shortened, fragmented PDMS chains are considered suitable for soil or clay mineral-induced degradation (*45*, *46*). Overall, the spectroscopic observations of DPI-HFP/Ecoflex 00-30 (Fig. 2, B to G) and DPI-HFP/Sylgard-184 (fig. S1, A to C) indicate that the material underwent Si─O cleavage by the F⁻ ion generated from DPI-HFP.

Decomposition kinetics of DPI-HFP/silicone composites

Verification of the kinetic parameters related to decomposition helps predict the degradation profile of the DPI-HFP/silicone composites, thereby enabling the design of transient silicone composites with diverse lifetimes. Therefore, kinetics analysis was performed under various thermal conditions to characterize the decomposition behavior of the DPI-HFP/silicone composite. Figure 3A and fig. S4 depict the decomposition of the DPI-HFP/Ecoflex 00-30 and DPI-HFP/Sylgard-184, respectively. Decomposition was triggered by applying 365 nm UV light for 30 min. Then, the decomposition rate was accelerated by heating at 120°C. In the decomposition process, the composites undergo a phase change from a cross-linked solid state to a de–cross-linked oily liquid state. Figure S5 depicts the degradation reaction images of DPI-HFP/Ecoflex 00-30 composites at various DPI-HFP concentrations [10, 20, and 30 weight% (wt%)]. It was observed that, when 10 wt% DPI-HFP was added, the quantity of UV-induced F⁻ ions was insufficient, leading to an inadequate degradation reaction. On the other hand, at 30 wt% concentration, the polymer degradation occurred effectively, but because of the excessive addition of DPI-HFP, the cross-linking of Ecoflex 00-30 did not occur sufficiently. As a result, the sample exhibited a gel-like behavior rather than hyperelastic, making it unsuitable for application in soft robotics. Therefore, we fabricated the robot based on the condition of adding 20 wt % DPI-HFP. Thermal analysis of the DPI-HFP/Ecoflex 00-30 composite using photo–differential scanning calorimetry (photo-DSC) was performed to determine the enthalpy required to decompose the composite and calculate the decomposition rate acceleration under various conditions (Fig. 3, B to D, and fig. S6, A to E). The decomposition reaction of the robot occurs at a constant temperature, so we measured the heat flow over time under constant

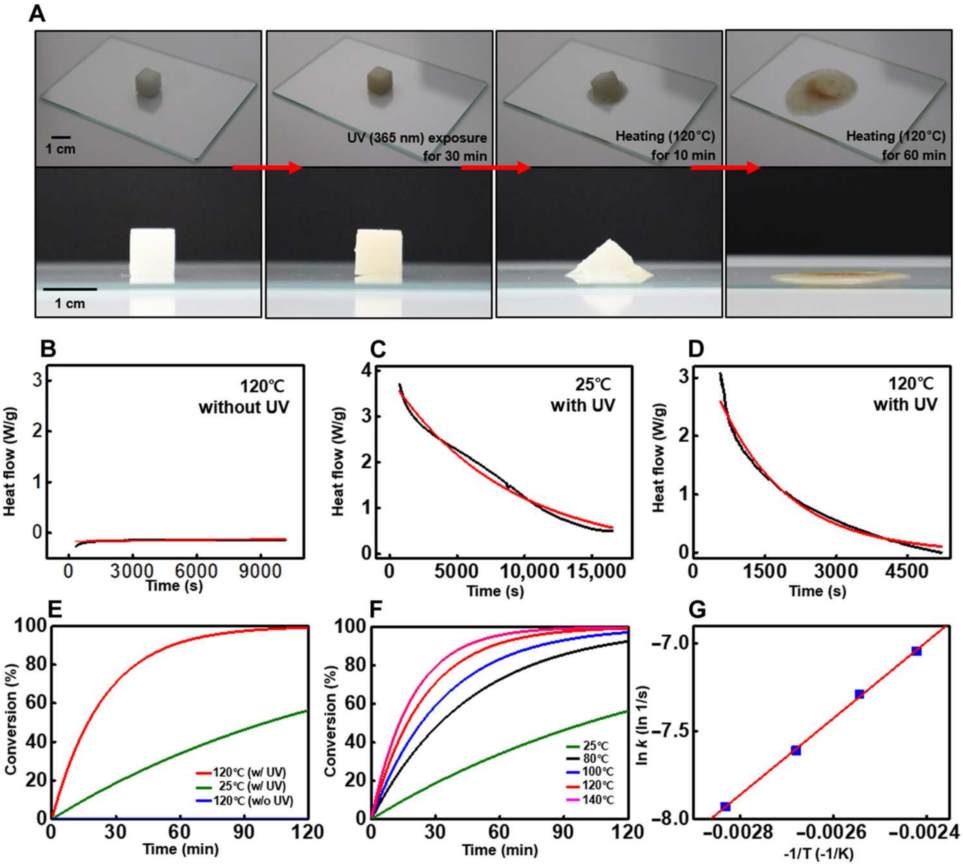

Fig. 3. Decomposition kinetics of the DPI-HFP/silicone composite. (**A**) Time-lapse photos showing decomposition of DPI-HFP/Ecoflex 00-30 triggered by exposure to UV (365 nm) for 30 min and followed by heating at 120°C for 1 hour. (**B**) Photo–differential scanning calorimetry (photo-DSC) curve of DPI-HFP/Ecoflex 00-30 at 120°C without UV exposure, revealing the stability of the composite without exposure to UV light (black, experimental data; and red, fitted data). (**C**) Photo-DSC curve of DPI-HFP/Ecoflex 00-30 at 25°C with UV exposure, revealing the UV-triggered transience of the composite (black, experimental data; red, fitted data). (**D**) Photo-DSC curve of DPI-HFP/Ecoflex 00-30 at 120°C with UV exposure, revealing the acceleration of decomposition upon exposure to heat (black, experimental data; red, fitted data). (**E**) DPI-HFP/Ecoflex 00-30 phase conversion under various conditions. Decomposition did not occur without exposure to UV light and increases as the temperature increases (120°C with UV, red; 25°C with UV, green; 120°C without UV, blue). (**F**) Phase conversion of DPI-HFP/Ecoflex 00-30 with UV radiation at different temperatures. Higher temperatures at decomposition resulted in faster decomposition rates (25°C, green; 80°C, black; 100°C, blue; 120°C, red; 140°C, magenta). (**G**) Arrhenius plot of DPI-HFP/Ecoflex 00-30 for calculating the kinetic parameters such as the activation energy (E_a) and reaction rate constant (*k*).

temperature conditions. Without applying the UV trigger, no heat flow was observed even at an elevated temperature of 120°C (Fig. 3B). In contrast, when UV light was applied (Fig. 3C), heat flow (~15,000 s) was observed even at room temperature (25°C) owing to the occurrence of an exothermic Si─O cleavage reaction. When UV light and 120°C heat were both applied (Fig. 3D), accelerated heat flow was observed (~4500 s).

The extent of phase conversion (α) of DPI-HFP/silicone can be measured via thermal analysis, considering the decomposition of DPI-HFP/silicone involves exothermic Si─O cleavage (*47*). Here, the value of α at time *t* is empirically quantified as

$$\alpha = \frac{\Delta H_t}{\Delta H_{\text{total}}} \quad (1)$$

where ΔH_{total} is the total amount of heat emitted during the decomposition and ΔH_{t} is the amount of heat emitted until time *t*. Photo-DSC analysis applied to Eq. 1 at various temperatures yielded decomposition profiles of DPI-HFP/Ecoflex 00-30, as shown in Fig. 3 (E and F). The decomposition of DPI-HFP/Ecoflex 00-30 was triggered by UV irradiation; therefore, external heating to 120°C without UV irradiation did not cause phase conversion. With prior application of a UV stimulus, the initial slope of the decomposition profile increased as the heating temperature increased, which indicated that external heat accelerates the decomposition reaction. This demonstrates that the overall reactions shown in Fig. 2A were accelerated by external heating after photolysis, because reactants with sufficient energy to overcome the activation energy barrier of the Si─O cleavage reaction became available.

Moreover, the model by Vyazovkin *et al.* (*48*) provides a theoretical expression relating α to the rate constant *k*

$$\alpha = 1 - e^{-kt} \quad (2)$$

Detailed derivations are provided in supplementary text S2, with fig. S5. Measuring α using photo-DSC and using it in Eq. 2 provide the value of *k* at each temperature (fig. S6), allowing us to generate an Arrhenius plot (Fig. 3G). The Arrhenius plot of the conversion rate, which is representative of the decomposition rate in the activation energy-based process, yields an Arrhenius pre-exponential factor $A = 0.1703$ and activation energy $E_a = 18.09$ kJ/mol, which facilitate the prediction of the degradation profile of DPI-HFP/Ecoflex 00-30 under UV radiation at arbitrary temperatures. The phase conversion datasets and Arrhenius plot for DPI-HFP/Sylgard-184 are shown in fig. 6. Kinetic analysis of DPI-HFP/Ecoflex 00-30 (Fig. 3) and DPI-HFP/Sylgard-184 (fig. S7) shows that these materials exhibit similar decomposition behavior. The analysis on the amount of F^- ions that vaporize without being consumed in fig. S8 is also investigated. The experiment was designed to capture the unreacted F^- ions released during the degradation process. As the polymer undergoes degradation, unreacted F^- ions are released and travel from the flask maintained at 120°C (fig. S8A, left). These F^- ions then condense and dissolve in the DI water contained within the cold flask (fig. S8A, right). In fig. S8B, the F^- ion concentration in the DI water was determined through ion chromatography analysis, revealing a value of 1020.74 mg/L for the 50 ml of DI water collected after decomposing a single gating robot. The quantified amount of unreacted and released F^- ion was found to be 51.04 mg (2.7×10^{-3} mol), which accounts for approximately 34% of the F^- ions initially included in one gaiting robot (DPI-HFP weighing 16.74 g, equivalent to 7.9×10^{-3} mol).

The decomposition behavior of identical DPI-HFP/Ecoflex 00-30 composite cubes (0.8 cm by 0.8 cm by 0.8 cm) under normal sunlight and UV-triggered conditions without additional heat exposure was analyzed (fig. S9). The energy transferred from sunlight was not sufficient to overcome the activation energy barrier to trigger decomposition; therefore, the DPI-HFP/Ecoflex 00-30 did not undergo a phase change without the designated trigger of UV light, which plays a key role in designing of reliable soft robots in real-world applications. In addition, this implies that the decomposition reaction can take place solely with the use of UV light, without the need for heat energy, as evidenced in fig. S9 and Fig. 3 (C and E).

Application to a soft robotic actuator

Hyperelastic silicone elastomers have been used extensively in the design of soft robots, considering that these materials allow various unconstrained movements. However, the stress concentration at the interface of silicone and DPI-HFP results in the formation of voids inside the material, which act as crack initiators and decrease the fracture strain (*49*, *50*). Incorporating a low volume fraction of DPI-HFP (maximum of 11.8 volume%, 20 wt% DPI-HFP/silicone elastomer) and a material preparation process using finely powdered DPI-HFP allows abundant network formation of the filler with the silicone elastomer matrix to retain the elastic modulus (*51*). We verified the conservation of the hyperelastic properties of the transient DPI-HFP/silicone composites via physical distortion and biaxial elongation tests and fabricated a gaiting soft robot. The physical distortion tests showed that the DPI-HFP/silicone had hyperelastic and tear-resistive mechanical properties (Fig. 4A) that originated from the silicone matrix. The tensile stress-strain evaluation of Ecoflex 00-30 and Sylgard-184 (Fig. 4B and figs. S10 and S11) showed that the composites undergo large elastic deformations before failure (Fig. 4B, DPI-HFP/Ecoflex 00-30; fig. S10, DPI-HFP/Sylgard-184). The addition of DPI-HFP to Ecoflex 00-30 decreased the fracture stress and strain (0 wt%, 0.4251 MPa, and 683.72%; 10 wt%, 0.1453 MPa, and 571.67%; and 20 wt%, 0.1897 MPa, and 493.34%) but did not change the elastic modulus (400% elastic limit and elastic modulus of 40.02 ± 1.65 kPa). Such mechanical properties are suitable for soft robotic applications and are highly superior to those of other stimulus-responsive composite materials reported, such as cyclic poly(phthalaldehyde) (cPPA)/photo-acid generator (PAG) (*31*).

We designed and fabricated a destructible on-demand pneumatic gaiting soft robot that takes advantage of the hyperelastic properties of the DPI-HFP/silicone composites. Figure 4C shows a schematic of our assembled robot (left) and an exploded view of its actuation components (right). The robot comprised a bending actuator with an air channel (DPI-HFP/Ecoflex 00-30), a strain limiter (DPI-HFP/Ecoflex 00-30), and four supporting feet (DPI-HFP/Sylgard-184). The dimensions of each component are shown in fig. S12. Figure 4D shows photographs (top) and corresponding finite element analysis (FEA) strain profiles (bottom) of the robot during pneumatic-actuated motion under pressures between 12 and −12 kPa. Applying pneumatic pressure to the air channel caused a bending motion induced by the difference in thickness and, in turn, the stiffness between the bending actuator and the strain limiter. The relatively rigid feet supported the structure robustly during

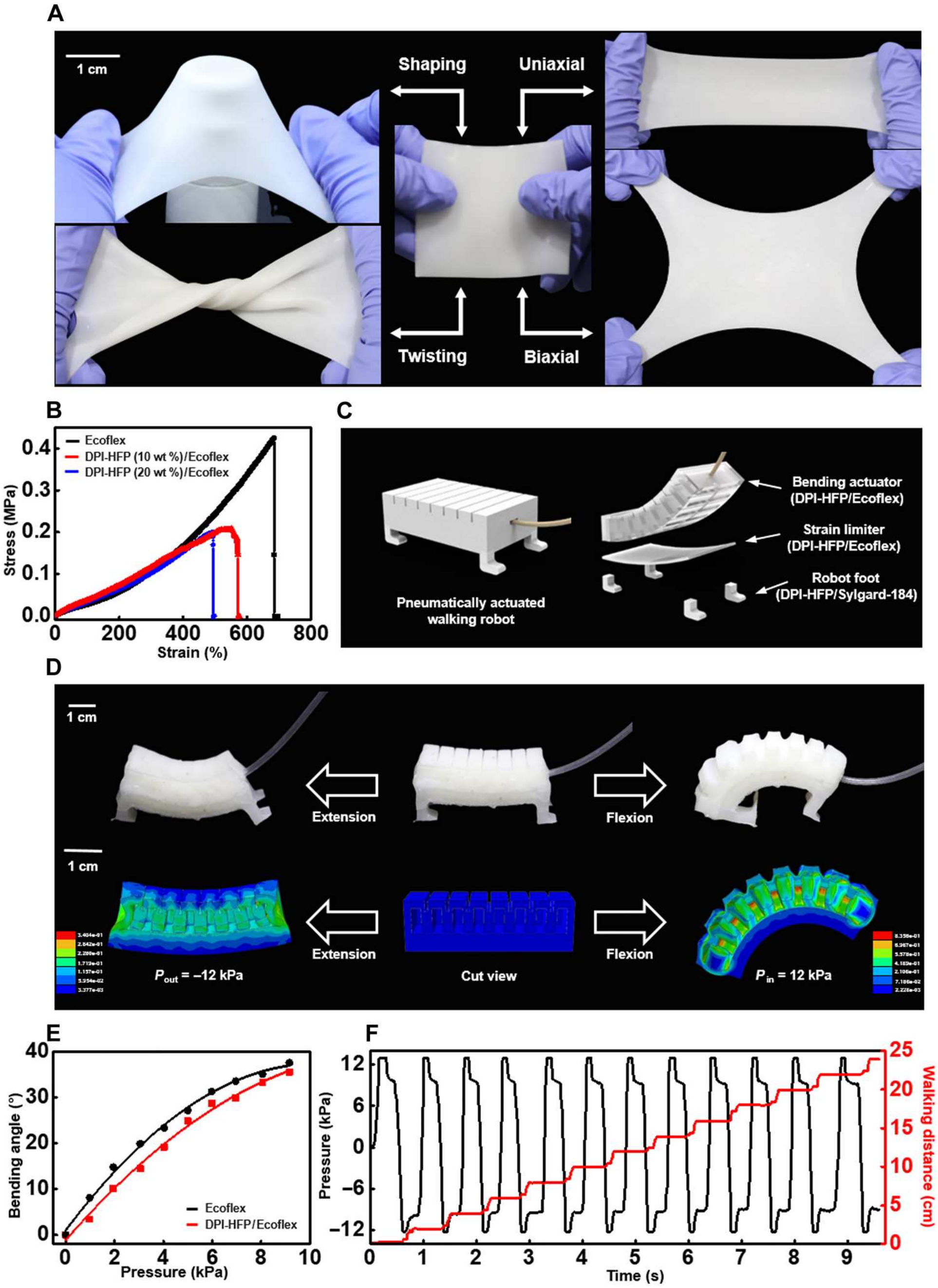

Fig. 4. Hyperelastic properties of DPI-HFP/silicone composites and application to a gaiting soft actuator. (**A**) Photos demonstrating the hyperelastic and tear-resistive properties of the composite under various strain conditions. (**B**) Stress-strain behavior of DPI-HFP/Ecoflex 00-30 composites at various DPI-HFP concentrations [0 weight% (wt%), black; 10 wt%, red; 20 wt%, blue]. (**C**) Schematics of the assembled (left) and exploded view (right) of a pneumatic gaiting actuator. (**D**) Photographs and simulated FEM-analyzed internal strain distributions of the gaiting soft robot during extension (left) and flexion (right) through pneumatic actuation. (**E**) Experimental measurements of the bending angle of an Ecoflex 00-30 actuator as a function of the inlet pressure with (20 wt%, red) and without (black) added DPI-HFP. (**F**) Locomotion distance (red) of the gaiting robot as a result of the cyclic pneumatic pressure (black).

movement and aided the robot in moving forward (*52*). When the robot was in a flexed state, the rear feet showed a higher frictional force compared to the front feet, which was attributed to their larger contact area with the ground. As a result, the robot moved forward during the transition to an extended state, given the greater displacement experienced by the front feet. FEA provided quantitative values for the actuation mechanism (Fig. 4D, cut view; fig. S13, bare view). The distribution of principal strains upon pressurization showed a maximum strain of 83.56% at the top wall of the air channel when the robot was in a flexed state. The bending angles of the pressurized Ecoflex 00-30 and DPI-HFP/Ecoflex 00-30 actuators were measured experimentally to demonstrate that adding a

DPI-HFP does not alter the original performance of a pure Ecoflex 00-30 (Fig. 4E). The Ecoflex 00-30 and DPI-HFP/Ecoflex 00-30 actuators exhibited similar bending angles at the same pressure. We observed the displacement of a DPI-HFP/silicone gaiting robot under cyclic pressure between 12 and −12 kPa (Fig. 4F). As a result, the robot moved steadily at a velocity of 2.5 cm/s through repeated extension and flexion.

Direct integration of multipurpose soft electronics

The integration of a multipurpose soft electronic system with a pneumatic soft robot expands the on-demand transient robot functionality to ambient condition monitoring, destructive condition detection and self-alarm, and actuation control. A temperature sensor array, strain sensor, and photodetector array were integrated with an on-demand transient robot fabricated from DPI-HFP/silicone composites. The strain sensor collected information about the strain induced during the walking motion of the robot and provided feedback about the motion data to control the robotic movement. The temperature sensor detected the ambient temperature, and the photodetectors detected UV light during regular operating conditions. Both the temperature sensor and photodetector served to monitor for the triggering conditions that initiate the destruction of the robot.

Figure 5A shows an image of the actual strain sensor and temperature sensor array integrated into the strain limiter of the robot and exploded view schematics. Both sensors comprised ~300 nm-thick copper layer deposited on a supportive polyimide (PI) dielectric film (~10 μm thick). Figure 5B shows the actual UV sensor array comprising PIN photodiodes installed on the forehead of the robot and its exploded view schematic; the array comprised a monocrystalline silicon membrane (~1500 nm thick) with a channel length of 20 μm and width of 625 μm and Cu (~300 nm thick) electrodes.

Figure 5C shows the fabricated strain sensor, which determines the strain by measuring the capacitance of the interdigitated electrodes, and a magnified view. Figure 5D shows the capacitance measured during a single cycle of robot walking, where the bending angle ranged from 0° to 35°. The sensors were designed such that an increase in capacitance was measured as the distance between the two neighboring electrodes increased (*53*). The strain induced in the region where the strain sensor was located was analyzed via finite element analysis (FEM), and the experimental data of the capacitance change were compared with the FEM data of the strain change at different bending angles (fig. S15A). Figure S15B shows the capacitance converted to strain. Figure 5E shows the continuous capacitance measurements of the strain sensor during robot walking. The capacitance change was consistently 1 pF under cyclical pneumatic pressurization between −10 and 10 kPa.

Figure 5F shows a magnified view of the temperature sensor array using the thermal resistivity of the material (*54*). The measured temperature coefficient of resistance of the copper was 2 milliohms $°C^{-1}$ in the temperature range of 25° to 100°C (Fig. 5G), which is comparable to the value reported in the literature (3.69 milliohms $°C^{-1}$) (*55*). Joule-heated rods at temperatures of 50°C, 70°C, and 100°C were placed under sensors 1, 3, and 5, respectively, and the temperatures across the surface resulting from heat diffusion were measured using an infrared camera (Fig. 5H, left) and the temperature sensor array (Fig. 5H, right). Temperature variations throughout the robot body, measured via the integrated temperature sensor array, corresponded to the calibrated temperature measurement shown in Fig. 5H (*56*).

Figure 5I shows the Si PIN (p-type/insulator/n-type) photodiode array and a magnified photodiode, which use the photoelectric current of a p-n junction to detect the UV light (*57*) that triggers the robot to disintegrate. Figure 5J shows the current-voltage (*I-V*) characteristics in both dark (without UV light) and bright (365 nm UV light) modes. The currents induced in dark and bright modes were 0 A and 3.4×10^{-8} A, respectively, under the applied voltage sweep from −2 to 2 V. When the UV light was cycled through on/off modes (0 to −2 V), the induced photocurrent was consistently -5×10^{-8} A at −2 V (Fig. 5K).

Demonstration of a lifetime configurable gaiting robot

Figure 6A shows the before and after images with respect to the destruction of the interfaced robot after the trigger (365 nm UV light, 120°C heating). The top row presents an integrated view of each sensor in the DPI-HFP/silicone robot. The bottom row shows images of the strain sensor, temperature sensors, and photodetectors that collapsed and entangled in an unusable and nonrestorable form with the destruction of the robot body. The transmittance of DPI-HFP/Ecoflex 00-30 to 365 nm wavelength light decreases as the thickness increases (fig. S17). Through the use of thin robot configurations with a thickness of less than 5 mm and sufficient light energy transfer using a powerful UV lamp, it was able to achieve the decomposition of the entire robot system. Furthermore, the electronic failure was assisted by the dissolution of the Cu used for the metal electrodes induced by the production of F^- ions during decomposition (*58*). Figure 6 (B to D) demonstrates the functional failures of the sensors to the nonrecoverable form, induced by the destruction of the robot. Figure 6B shows a robust change in the strain sensor capacitance before failure owing to robot body instability during decomposition. Figure 6C shows the stable resistance reading of 0 ohms from the temperature sensor before the robot was triggered, which rapidly exceeded 10^6 ohms as the robot was triggered with UV light and heat. In addition, Fig. 6D shows that the induction of photocurrent (-5×10^{-8} A at −2 V) was disabled as the robot collapsed. Figure S18 provides an in-depth review of the Cu degradation mechanism. Figure S18A depicts the Cu etching process initiated by the generation of F^- ions from the degradation of the DPI-HFP/Ecoflex 00-30 composite. It is well established that, when Cu reacts with F^- ions at elevated temperatures, CuF_2 is formed (*59*). Figure S18 (B and C) demonstrates the failure of the Cu resistor specimen following the triggering (365 nm UV light, 120°C heating) with the DPI-HFP/Ecoflex 00-30 composite. Figure S18B exhibits the presence of broken circuits, while fig. S18C illustrates real-time monitoring of resistance, showcasing a rapid increase in resistance exceeding 10^6 ohms. Figure S18D provides optical microscope images of the resistor specimen before and after the experiment. Circular-shaped etched pits, induced by the presence of F^- ions, can be observed within the Cu lines. These pits contribute to the failure of the resistor specimen.

We operated the gaiting soft robot with various electronics under an arbitrary set of conditions and ultimately triggered its disintegration. To demonstrate its functionality, the robot was deployed on a series of hypothetical military missions, including scouting a foreign environment without exposure to unwanted parties, recognizing the decomposition risk factors, escaping to avoid destruction, and finding a triggerable environment for the

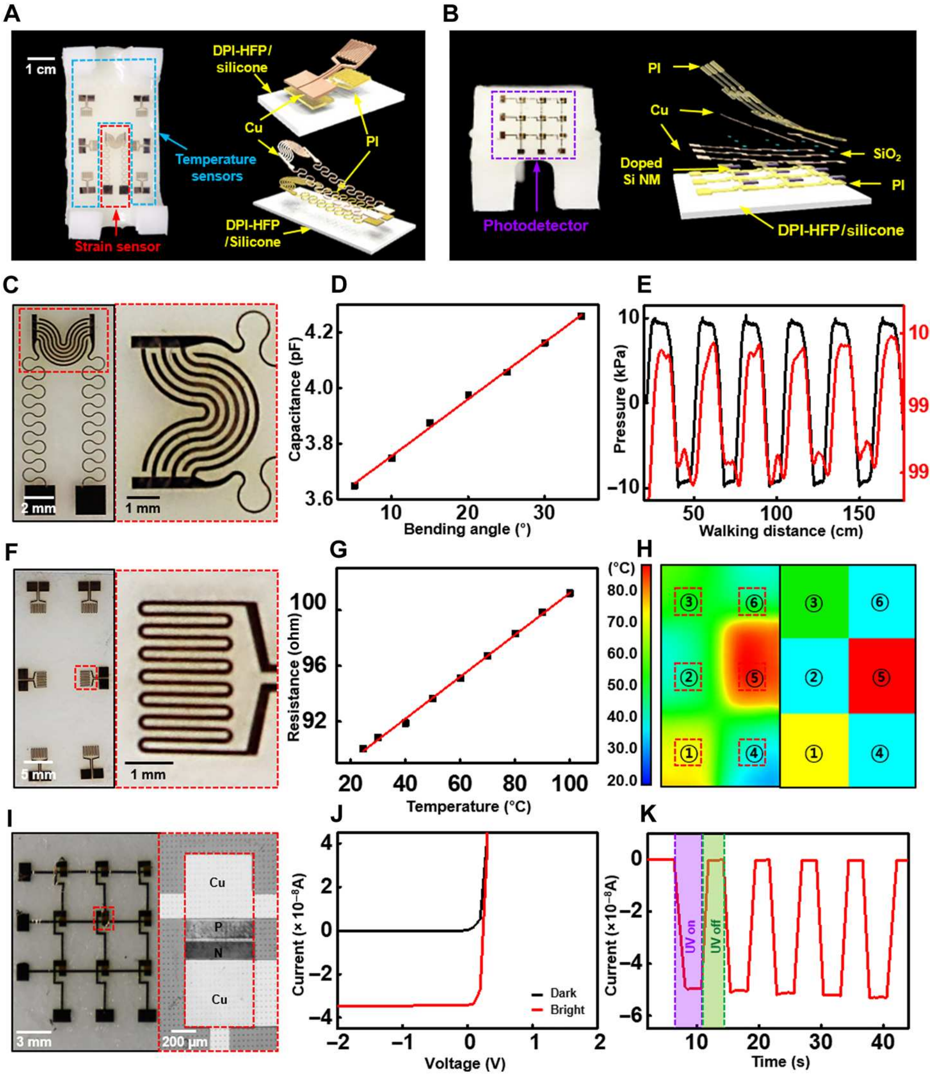

Fig. 5. Direct integration of multipurpose sensors onto the transient soft actuator. (**A**) Temperature and strain sensors integrated into the soft actuator (left); exploded view of both sensors (right). (**B**) Photodetector array integrated into the soft actuator (left); exploded view of the photodetector array (right). (**C**) Cu strain sensor with 200 μm-wide electrode traces. (**D**) Variation in the strain sensor capacitance as the bending angle increases (0° to 35°). (**E**) Capacitance change in the strain sensor under cyclical pneumatic pressurization between −10 and +10 kPa. (**F**) Cu temperature sensor with 200 μm-wide electrode traces. (**G**) Resistance variation of the Cu temperature sensor as the ambient temperature increases. A coefficient of resistance of 0.2 ohms $°C^{-1}$ for 25°C to 100°C was measured from the plot. (**H**) Localized temperature variations of Cu resistive sensors with Joule-heated rods placed directly below (sensor 1: 50°C, sensor 3: 70°C, and sensor 5: 100°C) measured by an infrared camera (left) and a resistive temperature sensor array (right). (**I**) A 3 × 3 array of PIN photodiodes comprising a silicon membrane with a 20 μm channel length and 625 μm width, and Cu electrodes. (**J**) Current-voltage (*I-V*) characteristics of a photodetector under dark (light off, black) and bright (365 nm UV light on, red) conditions. (**K**) Photodiodic behavior during cycling UV on and off states. A current of -5×10^{-8} A is induced at −2 V and no current flows at 0 V.

transient DPI-HFP/silicone–based gaiting robot to self-disintegrate (Fig. 6, B and C, and movie S1). First, the robot entered Zone 1 (60°C via a heat gun) and collected information regarding the temperature of the environment. Then, the robot entered zone 2 (365 nm UV light on) and collected information regarding the UV light in the environment. The material transience began at this point due to the UV light trigger. When the robot entered zone 3 (120°C via hot plate), it noted the hazardous risk of accelerated decomposition owing to the high temperature and warned the operator to escape the zone quickly. After the entire mission was complete, the robot entered the final zone (120°C via a hot plate) and rapidly decomposed into an oily liquid state within 1 hour, leaving no potential for recovery.

Closed-loop trigger disintegration system of gaiting soft robot

Utilizing the DPI-HFP/silicone composite whose decomposition can be triggered by the UV (365 nm) light, we have formed a closed-loop system by integrating UV light-emitting diodes (LEDs) and Joule heater. In the following demonstration, we were able to remotely initiate the material to autonomously self-decompose after the missions through a closed-loop system of self UV triggering and heating. In Fig. 7A, the exploded view in the center

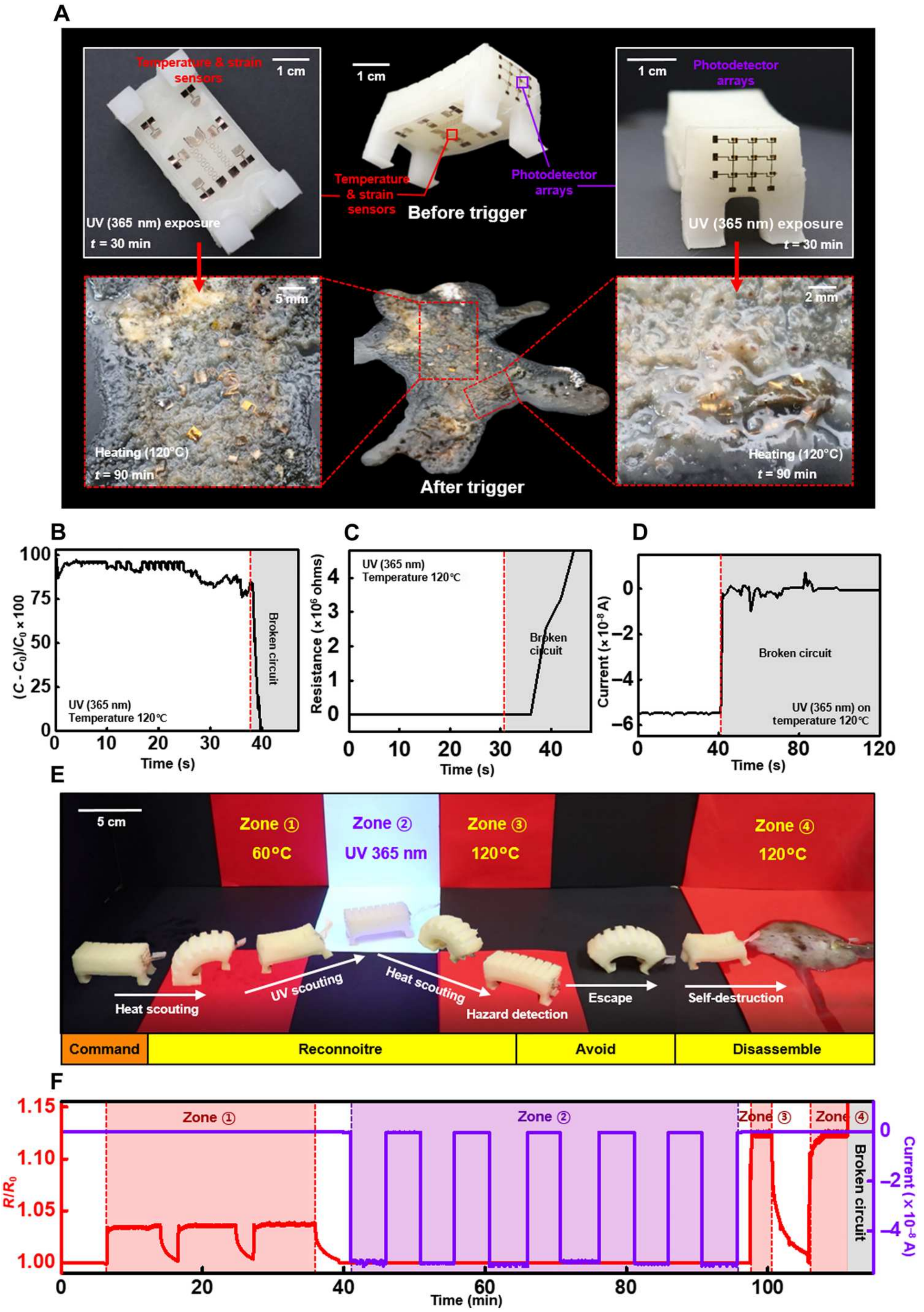

Fig. 6. Autonomic operation of a lifetime controlled gaiting robot. (**A**) Photographs of the gaiting robot before and after decomposition at 120°C triggered by 30 min of UV (365 nm) exposure. (**B**) Time-dependent changes in capacitance measured by the strain sensor. Transient behavior is observed when the capacitance reading is disabled. (**C**) Time-dependent changes in resistance measured by the temperature sensor. Transient behavior is observed when the resistance rapidly increases to 10^6 ohms. (**D**) Time-dependent changes in the photocurrent measured by the photodetector array. Transient behavior is observed when the induced photocurrent reaches 0 A. (**E**) Time-lapse images of the gaiting robot with integrated electronic devices. The robot enters the heat zone (zone 1, 70°C) and UV trigger zone (zone 2, 365 nm) to gather temperature and UV light information. When the robot enters the high-temperature zone (zone 3, 120°C), the embedded temperature sensor allows the robot to recognize accelerated decomposition conditions and escape from the hazardous zone. Once the robot decides to terminate its existence, it enters the final heat zone (zone 4, 120°C) to disassemble. (**F**) In situ measurement of temperature and UV light from the robot via embedded temperature sensor and photodetector. The conditions of the temperature and UV light correspond to the zones that the robot explored.

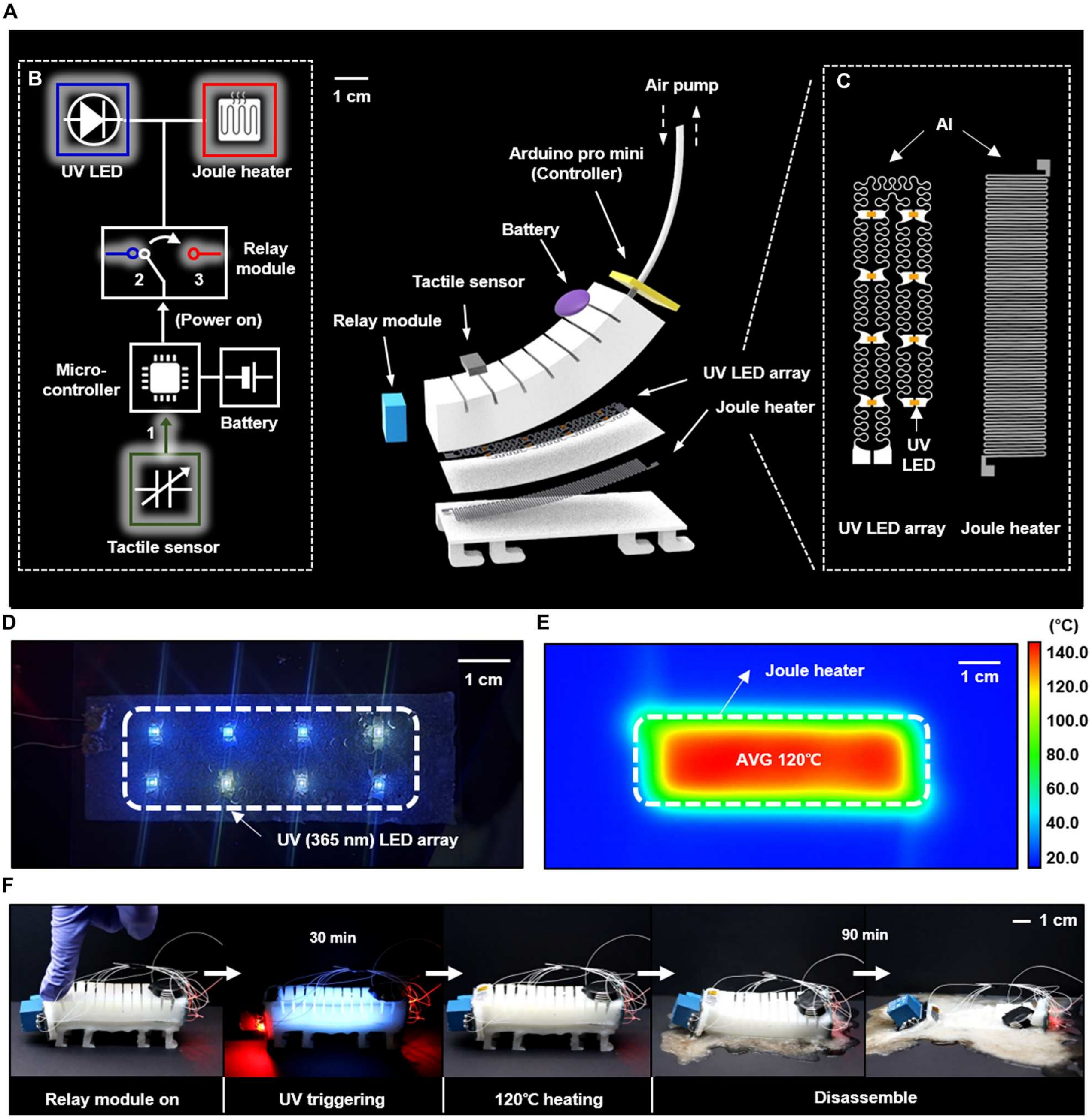

Fig. 7. Closed-loop trigger induced disintegration system of gaiting soft robot. (**A**) Overall scheme and exploded view of the closed-loop trigger induced disintegration system for a transient gaiting soft robot. (**B**) Schematic explanation of the operating principle and electrical circuit diagram of the closed-loop trigger disintegration system. (**C**) Schematic image of the UV LED array and Joule heater operated by the system. (**D**) Photograph of the UV LED array operated by the Arduino microcontroller and relay module. (**E**) Thermal image of automatically activated Joule heater by Arduino microcontroller and relay module. (**F**) Sequential images demonstrating the application of the actual closed-loop trigger disintegration system to the soft robot.

reveals the robot's composition, where an Al foil joule heater is attached to the strain limiter section of the robot, with a DPI-HFP/Ecoflex 00-30 passivation layer placed on top of it. An array of UV LEDs is connected through Al wires on this layer. The head section of the bending actuator is equipped with an Arduino Pro Mini microcontroller, and coin batteries (total of 6 V) is connected to supply the power to the system's operation. The tail section of the bending actuator integrates a relay module to control the UV mode and heating mode, along with a capacitive touch tactile sensor providing real-time feedback to the microcontroller. Figure 7B presents a schematic explanation of the operating principle of the closed-loop trigger disintegration system. When the capacitance of the capacitive touch sensor rapidly drops below the set point, power is supplied to the relay module, and the UV LEDs turn on. After UV triggering for 30 min, the switch inside the relay module is activated by the signal from the microcontroller, and the Joule heater operates for approximately 1.5 hours until full degradation. Figure 7C represents the schematic image of the UV LED array and Joule heater operated by the system. The UV LED array was constructed by connecting eight LEDs to Al electrodes. Because the strain limiter undergoes significant deformation during the robot's walking motion, the Al electrodes were fabricated in a serpentine structure to prevent wire breakage due to deformation. The Joule heater was implemented in a resistor-type configuration by utilizing laser cutting on an Al foil (line width of 4 μm), and it was integrated into the soft robot.

Figure 7 (D and E) demonstrates the operation of the UV LED array and Joule heater through the closed-loop trigger disintegration system, respectively. When a little pressure is applied to the capacitor-type tactile sensor, an instantaneous discharge occurs, resulting in a momentary decrease in capacitance value. This change is detected in real time by the Arduino microcontroller. Once the capacitance value falls below the predefined set point, the relay module activates the UV LEDs (Fig. 7D). After 30 min of UV LED operation, the microcontroller automatically generates a signal that switches on the relay module and activates the Joule heater (Fig. 7E). In the IR images, the Joule heater is heated up to a maximum temperature of approximately 140°C, with an overall average temperature of around 120°C, which could induce the material's decomposition.

Figure 7F consists of sequential images demonstrating the application of the actual closed-loop trigger disintegration system to the gaiting soft robot. The relay module is activated by touching the tactile sensor, as shown in the second image, causing the UV LEDs inside the robot to operate. After 30 min, the Joule heater is initiated and heated up to 140°C and accelerates the disintegration reaction of the robot's frame. After approximately 90 min, as depicted in the image on the far right, most of the soft robot undergoes disintegration, leaving only the components used for the closed-loop trigger disintegration system. Videos demonstrating the walking actuation and decomposition reaction of the soft robot with the integrated closed-loop trigger disintegration system are available in movies S2 and S3, respectively. Through the implementation of this untethered closed-loop trigger disintegration system, the potential applicability in real-world operating environments for soft robotics is demonstrated.

DISCUSSION

The proposed DPI-HFP/silicone composites enable a novel mechanism for on-demand material decomposition initiated by UV exposure while maintaining the highly elastic and stretchable mechanical properties of conventional silicone elastomers used in soft robots. The FTIR and NMR analyses conducted after UV exposure revealed the sequential chemistry involved in the photo-generation of F⁻ ions from DPI-HFP and the subsequent decomposition of Si─O─Si bonds. These findings suggest a backbone cleavage mechanism of silicone composites due to the presence of generated fluoride ions. The temperature-dependent kinetics were analyzed by photo-DSC, and the increasing rate of accelerated decomposition with the increase in temperature was determined on the basis of the Arrhenius equation.

A largely deformable and on-demand disintegrating pneumatic gaiting soft robot was designed and fabricated by combining DPI-HFP/Ecoflex 00-30 and DPI-HFP/Sylgard-184 composites, thereby demonstrating the usability of our novel material for soft robotics applications. Embedding the robot with flexible electronics in the form of strain, temperature, and UV light sensors successfully provided multifunctionality for controlling robotic motion, scouting the surrounding environment, and self-diagnosing a triggerable condition to choose self-protection or self-destruction.

While it is assumed that the F^- ions generated during the decomposition reaction are consumed for Si─O bond scission, there are still concerns about their potential residues or unreacted species. Upon dismantling a single gaiting robot, we observed the generation of 51.04 mg of F^- ions. This amount corresponds to approximately 1.14 to 2.28% of the lethal dose recommended for an adult male weighing 70 kg, as per safety guidelines (fig. S8). To further enhance safety use, we conducted additional experiments to reduce the amount of F^- ions released by using $CaCl_2$ as a neutralizer (fig. S8). $CaCl_2$ is widely used as an F^- mediator, capable of neutralizing F^- ions and producing CaF_2 (*42*). The gaiting robot made of 20 wt% DPI-HFP with Ecoflex 00-30 was coated with two different concentrations (10 and 100 g/L) of $CaCl_2$ solutions in DI water. Each concentration resulted in reduced levels of F^- ions being released, with 8.5×10^{-4} mol released at 10 g/L and 1.9×10^{-4} mol released at 100 g/liter, respectively. In case of the robot coated with $CaCl_2$ solutions (10 g/liter), 8.5×10^{-4} mol of F^- ions are released, which accounts for 7.37% of the total F^- ions released from input DPI-HFP. For $CaCl_2$-coated sample (100 g/L), even more reduced F^- ions are generated (1.9×10^{-4} mol), which accounts for approximately 2.44% of the total F^- ions generated. This result indicates that $CaCl_2$ could effectively mitigate the F^- ion release. However, it is still important to exercise caution when handling and disposing of such materials to ensure proper safety measures. In addition, further research on the environmental impact of the residues and strategies for managing them safely could expand the field of on-demand transient robotics application.

MATERIALS AND METHODS

Preparation of DPI-HFP/silicone composite

The required amount of diphenyl iodonium hexafluorophosphate (DPI-HFP; TCI, Japan) for a 1:1 mass ratio was added to Ecoflex 00-30 prepolymer (Smooth-On, USA), followed by manual stirring using a metal stick to prepare DPI-HFP/Ecoflex 00-30 resin. Then, the mixture was placed in a vacuum desiccator for 5 min to remove air bubbles. The mixture was poured into a three-dimensionally (3D) printed mold and cured in an oven at 60°C for 30 min. The same procedure was followed to prepare the DPI-HFP/Sylgard-184 composite using Sylgard-184 (Dow Corning, USA), except that the prepolymer was in a 20:1 ratio and curing was performed for 60 min. To prepare the DPI-HFP/PDMS composite used for residue analysis, trimethyl-terminated PDMS (M.W. = 139,000; Alfa Aesar, USA) was mixed with 20 wt% DPI-HFP.

Characterization and decomposition analysis of DPI-HFP/silicone composites

To determine the mechanical properties of the DPI-HFP/silicone composites, uniaxial tensile tests were performed using an Instron 3343 universal testing machine (Instron, USA) with a fixed receding strain rate of 10%/s. We used a VL-215 L model (Vilber Lourmat, France) consisting of a 15 W tube, which emits an intensity of 2300 $\mu W/cm^3$ at a distance of 15 cm, for the UV lamp required for the decomposition reaction. A Nicolet iS50 FTIR spectrophotometer (Thermo Fisher Scientific, USA) was used for decomposition chemistry analysis. ^{29}Si- and ^{1}H-solid-state NMR data were obtained using a 500 MHz Avance III system (Bruker, Germany), and solution-state ^{29}Si-NMR data were obtained using a 600 MHz Avance 600 system (Bruker, Germany) with tetrahydrofuran as the solvent. GPC measurements were obtained with a Shodex SEC LF-804 column with a Wyatt OptiLab T-rEx refractive index detector, with chloroform as the solvent. Decomposition kinetics were measured using a photo-DSC system comprising a DSC-Q200 (TA Instruments, USA) and an Omnicure-s2000 spot-cure light source (Excelitas, USA).

Fabrication, characterization, and simulation of soft robots

The robot bending actuator and feet were formed by curing DPI-HFP/Ecoflex 00-30 and DPI-HFP/Sylgard-184 in 3D printed PLA molds. Then, the uncured DPI-HFP/Ecoflex 00-30 was applied at the interfaces between each part of the integrated robot and cured at 60°C for 30 min to act as an adhesive. A small hole was drilled in the body using a needle, and a tube was inserted for pneumatic actuation. The displacement and bending angle of the robot were characterized using image analysis software (Tracker 5.1.5, Open Source Physics), whereas the pneumatic pressure was measured using a customized Arduino setup comprising a pressure sensor and a microcontroller.

The motions of the transformable robot were simulated via 3D FEA using commercial software (ABAQUS, Dassult Systemes, France). The main body part of the transformable robot was developed with an inner empty space to model air pressure. In the empty space, a uniform pressure was applied to the walls perpendicular to the inner surface without air injection holes. The element type was a four-node linear tetrahedron (C3D4). The elastic modulus, Poisson's ratio, and density were set to 40 kPa, 0.43, and 1.07 g/cm^3, respectively, which corresponded to the mechanical properties of DPI-HFP/Ecoflex 00-30.

A closed environmental experiment for F$^-$ ion subaquatic trapping

A closed environmental experiment is designed to capture the vaporized F$^-$ ions during the degradation process of the DPI-HFP/Ecoflex 00-30 sample. This experiment involved the use of a sealed flask placed on a hot plate and a vial containing DI water immersed in an ice water bath (fig. S8). The designed experiment facilitates the convection by using the temperature difference (120°C) between the hot flask and the cold vial. The temperature gradient allowed the F$^-$ ions to effectively migrate from the hot flask and condensed into the DI water inside the cold vial. For the coating process, the gaiting robot was immersed in the solutions of different concentrations (10 and 100 g/L) of CaCl$_2$ in DI water. Then, the coated robot was dried inside a 70°C oven for 1 hour.

Fabrication of multipurpose electronic sensors

Figures S14 and S16 illustrate the electronics fabrication processes for the temperature, strain, and UV light sensors. The fabrication of temperature sensors and strain sensors began by laminating a PI film (10 μm, Goodfellow) onto a DPI-HFP/Ecoflex 00-30 (~500 μm)–coated glass slide. A thin film of copper (Cu, 300 nm) was deposited on the PI via sputtering. Laser cutting of the PI-Cu bilayer defined the resistive structure for the temperature sensor and capacitive structure for the strain sensor. The DPI-HFP/Ecoflex 00-30 with embedded sensors was removed from the glass slide and adhered onto the DPI-HFP/Ecoflex 00-30 robot.

To fabricate the photodiode array, a SiO$_2$ diffusion mask was deposited on a silicon on insulator (SOI) wafer (top Si thickness of ~1500 nm, p-type, Soitec) via plasma-enhanced chemical vapor deposition. The diffusion doping of boron (spin-on-dopant 20B, Filmtronics; tube furnace at 1050°C with N$_2$ flow) and phosphorous (spin-on-dopant P509, Filmtronics; tube furnace at 1000°C with N$_2$ flow) through the SiO$_2$ diffusion mask yielded Si membrane PIN diodes. The buried oxide was removed by applying HF acid into the hole pattern (diameter, ~5 μm) that was dry etched with reactive ion etching (SF$_6$, 15 sccm (standard cubic centimeter per minute), 200 W). The removal of the buried oxides allowed the top monocrystalline Si membrane to be released and transferred onto a diluted PI (D-PI) membrane [converted from poly(pyromellitic dianhydride-*co*-4,4-oxydianiline), ~1.5 μm, Sigma-Aldrich] on a sacrificial poly(methyl methacrylate) (PMMA)–coated (~600 nm, Microchem) silicon wafer. Electrical connections and contact pads (Cu, ~300 nm) were formed by sputtering and liftoff procedures. D-PI was spin-coated over the diode array and photopatterned to dry etch the excessive D-PI layout. Furthermore, PMMA removal via immersion in acetone allowed the PIN diode array to be released and transferred onto the DPI-HFP/Ecoflex 00-30 robot body.

Fabrication of closed-loop trigger disintegration system

The autonomous robot system consists of a microcontroller (Arduino Pro Mini 328 5 V/16 MHz), a coin cell (Bexel XX 3 V), a capacitive touch sensor, a relay module (1Ch 5 V, SRD-05VDC-SL-C), a UV LED (VLMU1610-365-135, Vishay, USA), and a Joule heater. The capacitive touch sensor, which provides real-time feedback to the microcontroller, experiences a momentary discharge when it comes into contact, causing the capacitance value to decrease. When the capacitance value rapidly drops below the set point, power is supplied to the relay module, and the UV LED turns on. After 30 min, the switch inside the relay module is activated by a signal from the microcontroller, and the Joule heater operates for approximately 2 hours before stopping.

Supplementary Materials

This PDF file includes:

Supplementary texts S1 and S2
Figs. S1 to S18
Legends for movies S1 to S3

Other Supplementary Material for this manuscript includes the following:

Movies S1 to S3

REFERENCES AND NOTES

1. C. Majidi, Soft robotics: A perspective—Current trends and prospects for the future. *Soft Robot.* **1**, 5–11 (2014).
2. M. Kovǎ, The bioinspiration design paradigm: A perspective for soft robotics. *Soft Robot.* **1**, 28–37 (2014).
3. G. M. Whitesides, Soft robotics. *Angew. Chem. Int. Ed. Engl.* **57**, 4258–4273 (2018).
4. P. Polygerinos, N. Correll, S. A. Morin, B. Mosadegh, C. D. Onal, K. Petersen, M. Cianchetti, M. T. Tolley, R. F. Shepherd, Soft robotics: Review of fluid-driven intrinsically soft devices;

manufacturing, sensing, control, and applications in human-robot interaction. *Adv. Eng. Mater.* **19**, 1700016 (2017).

5. A. Sadeghi, A. Tonazzini, L. Popova, B. Mazzolai, A novel growing device inspired by plant root soil penetration behaviors. *PLOS ONE* **9**, e90139 (2014).
6. A. Sadeghi, A. Mondini, B. Mazzolai, Toward self-growing soft robots inspired by plant roots and based on additive manufacturing technologies. *Soft Robot.* **4**, 211–223 (2017).
7. M. Liu, S. Zhu, Y. Huang, Z. Lin, W. Liu, L. Yang, D. Ge, A self-healing composite actuator for multifunctional soft robot via photo-welding. *Compos. Part B. Eng.* **214**, 108748 (2021).
8. S. Terryn, J. Brancart, D. Lefeber, G. Van Assche, B. Vanderborght, Self-healing soft pneumatic robots. *Sci. Robot.* **2**, eaan4268 (2017).
9. H. Bai, Y. S. Kim, R. F. Shepherd, Autonomous self-healing optical sensors for damage intelligent soft-bodied systems. *Sci. Adv.* **8**, eabq2104 (2022).
10. Y. Yang, Y. Li, Y. Chen, Principles and methods for stiffness modulation in soft robot design and development. *Bio-Des. Manuf.* **1**, 14–25 (2018).
11. J. W. Boley, W. M. van Rees, C. Lissandrello, M. N. Horenstein, R. L. Truby, A. Kotikian, J. A. Lewis, L. Mahadevan, Shape-shifting structured lattices via multimaterial 4D printing. *Proc. Natl. Acad. Sci. U.S.A.* **116**, 20856–20862 (2019).
12. B. Mazzolai, C. Laschi, A vision for future bioinspired and biohybrid robots. *Sci. Robot.* **5**, eaba6893 (2020).
13. F. Hartmann, M. Baumgartner, M. Kaltenbrunner, Becoming sustainable, the new frontier in soft robotics. *Adv. Mater.* **33**, 2004413 (2021).
14. Defence Advanced Research Projects Agency (DARPA), "Vanishing acts: A call for disappearing delivery vehicles" (2015).
15. M. Lucia, "Someday disposable drones may deliver a payload, then vanish," *NPR*, 2 March 2017.
16. C. A. Aubin, S. Choudhury, R. Jerch, L. A. Archer, J. H. Pikul, R. F. Shepherd, Electrolytic vascular systems for energy-dense robots. *Nature* **571**, 51–57 (2019).
17. R. K. Katzschmann, J. DelPreto, R. MacCurdy, D. Rus, Exploration of underwater life with an acoustically controlled soft robotic fish. *Sci. Robot.* **3**, eaar3449 (2018).
18. G. Muscato, F. Bonaccorso, L. Cantelli, D. Longo, C. D. Melita, Volcanic environments: Robots for exploration and measurement. *IEEE Robot. Automat. Mag.* **19**, 40–49 (2012).
19. J. Huo, M. Liu, K. A. Neusypin, H. Liu, M. Guo, Y. Xiao, Autonomous search of radioactive sources through mobile robots. *Sensors (Basel).* **20**, 3461 (2020).
20. R. R. Murphy, J. Peschel, C. Arnett, D. Martin, in *2012 IEEE International Symposium on Safety, Security, and Rescue Robotics (SSRR)* (IEEE, 2012), pp. 1–4.
21. C. García-Garrido, L. A. Pérez-Maqueda, J. M. Criado, P. E. Sánchez-Jiménez, Combined kinetic analysis of multistep processes of thermal decomposition of polydimethylsiloxane silicone. *Polymer* **153**, 558–564 (2018).
22. P. Hu, J. Madsen, A. L. Skov, One reaction to make highly stretchable or extremely soft silicone elastomers from easily available materials. *Nat. Comm.* **13**, 370 (2022).
23. H. J. Qi, M. C. Boyce, Stress–strain behavior of thermoplastic polyurethanes. *Mech. Mater.* **37**, 817–839 (2005).
24. L. Feng, S. Li, S. Feng, Preparation and characterization of silicone rubber with high modulus via tension spring-type crosslinking. *RSC Adv.* **7**, 13130–13137 (2017).
25. S. Walker, J. Rueben, T. Van Volkenburg, S. Hemleben, C. Grimm, J. Simonsen, Y. Mengüç, Using an environmentally benign and degradable elastomer in soft robotics. *Int. J. Intell. Robot. Appl.* **1**, 124–142 (2017).
26. M. Baumgartner, F. Hartmann, M. Drack, D. Preninger, D. Wirthl, R. Gerstmayr, L. Lehner, G. Mao, R. Pruckner, S. Demchyshyn, L. Reiter, M. Strobel, T. Stockinger, D. Schiller, S. Kimeswenger, F. Greibich, G. Buchberger, E. Bradt, S. Hild, S. Bauer, M. Kaltenbrunner, Resilient yet entirely degradable gelatin-based biogels for soft robots and electronics. *Nat. Mater.* **19**, 1102–1109 (2020).
27. G. Lee, Y. S. Choi, H.-J. Yoon, J. A. Rogers, Advances in physicochemically stimuli-responsive materials for on-demand transient electronic systems. *Matter* **3**, 1031–1052 (2020).
28. O. Shelef, S. Gnaim, D. Shabat, Self-immolative polymers: An emerging class of degradable materials with distinct disassembly profiles. *J. Am. Chem. Soc.* **143**, 21177–21188 (2021).
29. A. Sagi, R. Weinstain, N. Karton, D. Shabat, Self-immolative polymers. *J. Am. Chem. Soc.* **130**, 5434–5435 (2008).
30. Q. E. A. Sirianni, E. R. Gillies, The architectural evolution of self-immolative polymers. *Polymer* **202**, 122638 (2020).
31. J. A. Kaitz, C. E. Diesendruck, J. S. Moore, End group characterization of poly(phthalaldehyde): Surprising discovery of a reversible, cationic macrocyclization mechanism. *J. Am. Chem. Soc.* **135**, 12755–12761 (2013).
32. J. L. Dektar, N. P. Hacker, Photochemistry of diaryliodonium salts. *J. Org. Chem.* **55**, 639–647 (1990).
33. Y. Yağci, I. Reetz, Externally stimulated initiator systems for cationic polymerization. *Prog. Polym. Sci.* **23**, 1485–1538 (1998).
34. S. Schlögl, M. Reischl, V. Ribitsch, W. Kern, UV induced microcellular foaming—A new approach towards the production of 3D structures in offset printing techniques. *Prog. Org. Coat.* **73**, 54–61 (2012).
35. Y. Yagci, F. Yilmaz, S. Kiralp, L. Toppare, Photoinduced polymerization of thiophene using iodonium salt. *Macromol. Chem. Phys.* **206**, 1178–1182 (2005).
36. J. H. Simons, ed., *Fluorine Chemistry* (Academic Press, 1954).
37. D. W. Davidson, S. K. Garg, The hydrate of hexafluorophosphoric acid. *Can. J. Chem.* **50**, 3515–3520 (1972).
38. M. J. Sailor, Chemical reactivity and surface chemistry of porous silicon, in *Handbook of Porous Silicon*, L. Canham, Ed. (Springer International Publishing, 2014), pp. 1–24.
39. C. E. Son, S.-S. Choi, Analytical techniques for measurement of crosslink densities of rubber vulcanizates. *Elastomers Compos.* **54**, 209–219 (2019).
40. H. Hara, Y. Sano, H. Mimura, K. Arima, A. Kubota, K. Yagi, J. Murata, K. Yamauch, Novel abrasive-free planarization of 4H-SiC (0001) using catalyst. *J. Electron. Mater.* **35**, L11–L14 (2006).
41. A. Isohashi, P. V. Bui, D. Toh, S. Matsuyama, Y. Sano, K. Inagaki, Y. Morikawa, K. Yamauchi, Chemical etching of silicon carbide in pure water by using platinum catalyst. *Appl. Phys. Lett.* **110**, 201601 (2017).
42. B. Rupasinghe, J. C. Furgal, Full circle recycling of polysiloxanes via room-temperature fluoride-catalyzed depolymerization to repolymerizable cyclics. *ACS Appl. Polym. Mater.* **3**, 1828–1839 (2021).
43. H. M. Brothers Jr., T. Boehmer, R. A. Campbell, S. Dorn, J. J. Kerbleski, S. Lewis, C. Mund, D. Pero, K. Saito, M. Wieser, W. Zoller, Determination of cyclic volatile methylsiloxanes in personal care products by gas chromatography. *Int. J. Cosmet. Sci.* **39**, 580–588 (2017).
44. D. J. Krug, M. Z. Asuncion, R. M. Laine, Facile approach to recycling highly cross-linked thermoset silicone resins under ambient conditions. *ACS Omega.* **4**, 3782–3789 (2019).
45. E. F. C. Griessbach, R. G. Lehmann, Degradation of polydimethylsiloxane fluids in the environment—A review. *Chemosphere* **38**, 1461–1468 (1999).
46. S. Xu, R. G. Lehmann, J. R. Miller, G. Chandra, Degradation of polydimethylsiloxanes (silicones) as influenced by clay minerals. *Environ. Sci. Technol.* **32**, 1199–1206 (1998).
47. S. Vyazovkin, A. K. Burnham, J. M. Criado, L. A. Pérez-Maqueda, C. Popescu, N. Sbirrazzuoli, ICTAC Kinetics committee recommendations for performing kinetic computations on thermal analysis data. *Thermochim. Acta.* **520**, 1–19 (2011).
48. R. Hardis, J. L. P. Jessop, F. E. Peters, M. R. Kessler, Cure kinetics characterization and monitoring of an epoxy resin using DSC, Raman spectroscopy, and DEA. *Compos. Part A Appl. Sci. Manuf.* **49**, 100–108 (2013).
49. S.-Y. Fu, X.-Q. Feng, B. Lauke, Y.-W. Mai, Effects of particle size, particle/matrix interface adhesion and particle loading on mechanical properties of particulate–polymer composites. *Compos. Part B Eng.* **39**, 933–961 (2008).
50. A. J. Kinloch, R. J. Young, *Fracture Behaviour of Polymers* (Kluwer Academic Publishers, 1983).
51. P. Mazurek, S. Vudayagiri, A. L. Skov, How to tailor flexible silicone elastomers with mechanical integrity: A tutorial review. *Chem. Soc. Rev.* **48**, 1448–1464 (2019).
52. Y. Tang, Y. Chi, J. Sun, T. H. Huang, O. H. Maghsoudi, A. Spence, J. Zhao, H. Su, J. Yin, Leveraging elastic instabilities for amplified performance: Spine-inspired high-speed and high-force soft robots. *Sci. Adv.* **6**, eaaz6912 (2020).
53. D. P. J. Cotton, I. M. Graz, S. P. Lacour, A multifunctional capacitive sensor for stretchable electronic skins. *IEEE Sens. J.* **9**, 2008–2009 (2009).
54. T. Dinh, H. Phan, A. Qamar, P. Woodfield, N. Nguyen, D. V. Dao, Thermoresistive effect for advanced thermal sensors: Fundamentals, design considerations, and applications. *J. Microelectromech. Syst.* **26**, 966–986 (2017).
55. J. H. Dellinger, The temperature coefficient of resistance of copper. *J. Franklin Inst.* **170**, 213–216 (1910).
56. T. P. Pearsall, M. A. Pollack, Compound semiconductor photodiodes, in *Semiconductors and Semimetals* (Elsevier, 1985), chap. 2, 173–245.
57. J.-Y. Bae, E.-J. Gwak, G.-S. Hwang, H. W. Hwang, D. J. Lee, J.-S. Lee, Y.-C. Joo, J.-Y. Sun, S. H. Jun, M.-R. Ok, J.-Y. Kim, S.-K. Kang, Biodegradable metallic glass for stretchable transient electronics. *Adv. Sci.* **8**, 2004029 (2021).
58. N. G. Mistkawi, M. A. Hussein, M. Ziomek-Moroz, S. B. Rananavare, Copper thin-film dissolution/precipitation kinetics in organic HF containing cleaning solution. *J. Electrochem. Soc.* **157**, 801–805 (2010).
59. M. A. Subramanian, L. E. Manzer, A "greener" synthetic route for fluoroaromatics via copper (II) fluoride. *Science* **297**, 1665 (2002).

Acknowledgments

Funding: This work was supported by the National Research Foundation of Korea (NRF) grants funded by the Korea government (NRF-2022M3H4A1A04096393 and NRF-2022R1C1C1008513). **Author contributions:** Conceptualization: M.-H.O., Y.-H.K., S.-M.L., S.Y.K., and S.-K.K. Methodology: M.-H.O., Y.-H.K., and S.-M.L. Investigation: M.-H.O., Y.-H.K., and S.-M.L.

Visualization: M.-H.O., Y.-H.K., S.-M.L., G.-S.H., K.-S.K., Y.-N.K., J.-Y.B., J.-Y.L., J.-Y.K., and Y.-C.K. Supervision: S.Y.K. and S.-K.K. Writing draft: M.-H.O., Y.-H.K., S.-M.L., and G.-S.H. **Competing interests:** The authors declare that they have no competing interests. **Data and materials availability:** All data needed to evaluate the conclusions in the paper are present in the paper and/or the Supplementary Materials.

Submitted 27 March 2023
Accepted 26 July 2023
Published 25 August 2023
10.1126/sciadv.adh9962

Science Advances

Lifetime-configurable soft robots via photodegradable silicone elastomer composites

Min-Ha Oh, Young-Hwan Kim, Seung-Min Lee, Gyeong-Seok Hwang, Kyung-Sub Kim, Yoon-Nam Kim, Jae-Young Bae, Ju-Young Kim, Ju-Yong Lee, Yu-Chan Kim, Sang Yup Kim, and Seung-Kyun Kang

Sci. Adv. **9** (34), eadh9962. DOI: 10.1126/sciadv.adh9962

Science Advances (ISSN 2375-2548) is published by the American Association for the Advancement of Science. 1200 New York Avenue NW, Washington, DC 20005. The title *Science Advances* is a registered trademark of AAAS.